

1 **Room temperature electron beam sensitive viscoplastic response of ultra-ductile**  
2 **amorphous olivine films**

3  
4 Andrey OREKHOV<sup>1,2</sup>, Nicolas GAUQUELIN<sup>2</sup>, Guillaume KERMOUCHE<sup>3</sup>, Alejandro GOMEZ-PEREZ<sup>4</sup>,  
5 Paul BARAL<sup>1,3</sup>, Ralf DOHMEN<sup>5</sup>, Michaël COULOMBIER<sup>1</sup>, Johan VERBEECK<sup>2</sup>, Jean Pierre RASKIN<sup>6</sup>,  
6 Thomas PARDOEN<sup>1,7</sup>, Dominique SCHRYVERS<sup>2</sup>, Jun LIN<sup>8</sup>, Patrick CORDIER<sup>9,10\*</sup>, Hosni IDRISSE<sup>1,2</sup>

7  
8 <sup>1</sup>Institute of Mechanics, Materials and Civil Engineering (IMMC), UCLouvain, B-1348, Louvain-la-  
9 Neuve, Belgium

10 <sup>2</sup>EMAT, University of Antwerp, Groenenborgerlaan 171, B-2020, Antwerp, Belgium

11 <sup>3</sup>Now at : Mines Saint-Etienne, Univ Lyon, CNRS UMR 5307LGF, Centre SMS, 158 Cours Fauriel,  
12 42023 Saint-Etienne, France

13 <sup>4</sup>NanoMegas SPRL, Boulevard Edmond Machtens 79, B1080 Brussels, Belgium

14 <sup>5</sup>Institut für Geologie, Mineralogie und Geophysik, Ruhr-Universität Bochum, D-44801 Bochum,  
15 Germany

16 <sup>6</sup>Institute of Information and Communication Technologies, Electronics and Applied Mathematics  
17 (ICTEAM), UCLouvain, B-1348, Louvain-la-Neuve, Belgium

18 <sup>7</sup>WEL research Institute, avenue Pasteur 6, 1300 Wavre, Belgium

19 <sup>8</sup>ICSM, CEA, CNRS, ENSCM, Univ Montpellier, Marcoule, France

20 <sup>9</sup>Univ. Lille, CNRS, INRAE, Centrale Lille, UMR 8207 - UMET - Unité Matériaux et Transformations,  
21 F-59000 Lille, France

22 <sup>10</sup>Institut Universitaire de France, F-75005 Paris, France

23

24 \* Corresponding author:

25 Patrick Cordier - [Patrick.cordier@univ-lille.fr](mailto:Patrick.cordier@univ-lille.fr) – (+33) 649 29 1879

26

27 Submitted to Acta Materialia – March 2024 – Revised July 2024 – Revised August 2024

28

29

30 **Highlights**

- 31 • At small scale and room temperature a-olivine is ductile with fracture strain up to 29 %  
32 • a-olivine becomes viscous and reaches much higher ductility under the electron beam  
33 accelerated at 80 kV and 200 kV  
34 • Radiolysis is the prominent mechanism that promotes ductility of a-olivine

35

36 **Abstract**

37 The mechanical properties of amorphous olivine (a-olivine) deformed at room temperature are  
38 investigated *in situ* in a TEM under uniaxial tension using a Push-to-Pull (PTP) device. Thin films  
39 of a-olivine were produced by pulsed laser deposition (PLD). With or without electron irradiation,  
40 a-olivine films deform plastically, with a gradual transition that makes impossible the  
41 determination of a precise threshold. The strength attains values up to 2.5 GPa. The increasing  
42 strain-rate in load control results in an apparent softening with stress drop. The fracture strain  
43 reaches values close to 30 % without e-beam irradiation. Under electron illumination at 200 kV,  
44 the strength is lower, around 1.7 GPa, while higher elongations close to 36 % are obtained.  
45 Alternating beam-off and beam-on sequences lead to exceptionally large fracture strains equal to  
46 68 % at 200 kV and 139 % at 80 kV. EELS measurements were performed to characterize the  
47 interaction between the electron beam and a-olivine. At a voltage of 80 kV, radiolysis  
48 accompanied by oxygen release dominates whereas at high voltage (300 kV) the interaction is  
49 dominated by knock-on type defects. Radiolysis is also the main interaction mechanism at 200 kV  
50 with low exposition which corresponds to most of our *in situ* TEM deformation experiments. To  
51 interpret the mechanical data, a simple 1D model has been developed to rationalize the load  
52 transfer between the PTP device and the specimen. The strain-rate sensitivity is 6 to 10 times  
53 higher when a-olivine is deformed under electron irradiation.

54 **Keywords:** Transmission electron microscopy; amorphous olivine; nanomechanical testing;  
55 electron irradiation

56

57

58 **1. Introduction**

59 Among silicate glasses, those with olivine composition (*i.e.*  $M_2SiO_4$  with  $M=Mg, Fe, Mn, \dots$ ) have  
60 been relatively little studied, largely due to the difficulty of preparing such samples by quenching  
61 from the melt [1]. The first reported observation of olivine glass was provided by Jeanloz *et al.* [2]  
62 from olivine specimens recovered from shock experiments at 56 GPa. The formation of this glass  
63 was then observed in static compression experiments in a laser-heated diamond anvil cell [3].  
64 Beyond the obvious importance of this composition in Earth sciences (olivine in its crystalline form  
65 is the main component of the Earth's upper mantle), the study of olivine glasses is of fundamental  
66 interest. Contrary to amorphous silica which is made of a polymerized network of  $SiO_4$  tetrahedra  
67 connected through their O vertices, amorphous olivine is dominated by isolated, non-polymerized  
68  $SiO_4$  tetrahedra, separated by  $M^{2+}$  polyhedra. More specifically, interest in this compound was  
69 revived when grain boundary amorphization was reported in olivine aggregate deformation  
70 experiments [4]. Stress amorphization of grain boundaries appears as a potential deformation  
71 mechanism under high stress [5], and in the particular case of olivine, this mechanism has been  
72 proposed as possibly being the cause of the drop in viscosity at the boundary between the  
73 lithosphere and the asthenosphere as the glass passes the glass transition temperature [6]. It  
74 therefore appears necessary to study the mechanical properties of olivine glasses. While glasses  
75 are usually brittle materials, it has been shown that ductility can be enhanced at small scales [7,8].  
76 This is particularly relevant in the case of amorphized grain boundaries, which can be nanometric  
77 in thickness.

78 In this study, we investigate the mechanical properties of amorphous olivine using  
79 micromechanical tensile tests in a transmission electron microscope (TEM). Recent works have  
80 shown that electron irradiation has a significant influence on the mechanical properties of  
81 amorphous silica [9], so particular attention is paid to this phenomenon.

82

83

84

85

## 86 2. Material and methods

### 87 *a. Pulsed Laser Deposition (PLD) of amorphous olivine ( $\alpha$ -olivine) films*

88 For the preparation of thin films, polycrystalline pellets of synthetic olivine with a nominal  
89 composition of  $\text{Fe}_{0.2}\text{Mg}_{1.8}\text{SiO}_4$  were ablated using a pulsed laser beam with a frequency of 10 Hz,  
90 a wavelength of 193 nm, and at a laser fluence of approximately  $5 \text{ J/cm}^2$ . Details on the setup can  
91 be found in Dohmen *et al.* [10]. The deposition rates were in the range 10-20 nm/min. The  
92 depositions were performed at a background vacuum pressure of  $1 \times 10^{-3} \text{ Pa}$  and at room  
93 temperature. Under these conditions, it has been demonstrated [10] that the silicate film of an  
94 olivine-like composition is amorphous and chemically homogeneous. The depositions were  
95 performed on clean [100] oriented silicon wafers. The resulting surface topography is small with  
96 a typical roughness of less than 1 nm [10], as measured by atomic force microscopy (AFM). The  
97 PLD set-up does not allow the rotation of the substrate during deposition and the plasma jet  
98 coming out of the target is relatively small compared to the substrate. This results in a deposited  
99 layer with some variation of the thickness (see Fig. 6c in [10]). The thickness has to be measured  
100 for every sample used for quantitative nanomechanical tensile testing *in situ* in the TEM for  
101 accurate estimation of the applied stress.

102

### 103 *b. TEM characterizations*

104 The initial microstructure was investigated on classical Focused Ion Beam (FIB) cross-sections of  
105  $\alpha$ -olivine deposited on a Si substrate. A Pt protection layer was deposited in two steps – by  
106 electron beam, then by ion beam– in order to minimize FIB damage at the sample surface. The  
107 FIB foils were thinned to a thickness  $< 50 \text{ nm}$ . An ion beam of 2 kV/0.2 nA was employed for final  
108 thinning of the specimen and to minimize irradiation damage generated during high-voltage FIB  
109 thinning. TEM characterizations were conducted in a FEI Osiris microscope equipped with highly  
110 efficient SuperX Energy Dispersive X-ray (EDX) system operated at 200 kV. Z-contrast images were  
111 recorded in scanning transmission electron microscope (STEM) mode with convergence angles of  
112 115-157 mrad using an HAADF-STEM detector. Selected area electron diffraction (SAED) patterns  
113 were used to calculate the “Reduced Pair Distribution Function”  $G(r)$  [11]. The *e-PDFSuite*  
114 software [12] was used for data reduction following a procedure detailed in Juhas *et al.* [12]. First

115 the data is azimuthally integrated in an equidistant Q-grid obtaining a 1D I(Q) graph that will be  
116 used for the final calculation. Since the sample was prepared as a FIB lamella, no further  
117 corrections-subtractions have to be performed because the interaction of the beam is only with  
118 the sample and not with any other container or support grid. The calculation of the structure  
119 function S(Q) and the derived one F(Q) are made exactly as described in [12] with the only  
120 difference of using the electron form factors instead of x-ray form factors. The r-poly function was  
121 used for background corrections of the F(Q), basically consisting on a n-degree polynomic fitting  
122 that has to take into account the shortest physical bond-distance in the sample and the  $Q_{MAXINST}$   
123 obtained during measurements. Then G(r) was calculated by normalization and Fourier  
124 transformation [13, 14]. The parameters applied for the Fourier transformation were: integral  
125 limits  $Q_{MAX} = 15 \text{ \AA}^{-1}$  and  $Q_{MIN} = 0.82 \text{ \AA}^{-1}$ ; R-grid plot in real space with 0.05 Å step from 0 to 10 Å.

126 Electron energy loss spectroscopy (EELS) was used to investigate the effect of e-beam  
127 irradiation on the a-olivine films. EELS measurements at 80 kV and 300 kV were performed on a  
128 Titan 80-300 double aberration corrected microscope equipped with a monochromator and a  
129 Gatan K2 direct electron detection camera (3710 pixels) mounted on a Gatan Quantum  
130 spectrometer. At 300 kV, the energy resolution was 0.5 eV at a dispersion of 0.25 eV/pixel used  
131 to record the O K, Fe L and Mg K edges simultaneously and 0.2 eV at a dispersion of 0.025 eV/pixel  
132 used to record the Si L edge. At 80 kV, the energy resolution was 0.3 eV at a dispersion of 0.15  
133 eV/pixel used to record the O K and Fe L edges simultaneously and 0.17 eV at a dispersion of  
134 0.025 eV/pixel used to record the Si L edge. EELS measurements at 200 kV were performed on a  
135 Titan 60-300 probe aberration corrected microscope equipped with a monochromator and a  
136 Gatan Enfinium spectrometer (2048 pixels), the energy resolution was 1 eV at a dispersion of 0.25  
137 eV/pixel used to record the O K and Fe L edges simultaneously and 0.2 eV at a dispersion of 0.025  
138 eV/pixel used to record the Si L edge. At each voltage, the dose was varied by changing the spot  
139 size from 14 to 17, as can be seen in Table 1, resulting in a slight defocus of the electron probe.  
140 The electron doses corresponding to those conditions are reported in Table 2. 600 spectra were  
141 acquired with an acquisition time of 0.2 s/spectra. For each measurement, a new fresh area of  
142 the sample was used. To maximize the visibility of the damage, the probe was kept at a constant  
143 position and spectra recorded as a function of time.

144

145 *c. in situ TEM nanomechanical testing*

146 Freestanding  $\alpha$ -olivine thin films have been produced in the context of another study [16]  
147 designed to perform nanomechanical tensile testing as shown in Fig. 1a. In the present work,  
148 undeformed freestanding beams were cut (Fig. 1b) using a dual-beam FIB/SEM instrument (FEI  
149 Helios Nanolab 650) equipped with an Omniprobe micromanipulator (Oxford Instruments plc,  
150 Tubney Woods, UK). Pt deposition was then used to attach the beam on a push-to-pull (PTP)  
151 device (PI 95 TEM PicoIndenter instrument from Bruker, see Fig. 1c) for *in situ* TEM tensile  
152 experiments [17, 18]. A dog bone shape was thus obtained by FIB (Fig. 1d). This approach allows  
153 avoiding FIB thinning that might alter the initial glassy microstructure and the resulting  
154 mechanical properties.

155 Quantitative tensile experiments with PTP were performed under load control mode. The  
156 applied force on the specimen was determined by removing the contribution of the PTP spring  
157 stiffness from the raw force. PTP stiffness was measured by performing a load-unload cycle after  
158 the tensile experiment (when the sample is broken). The engineering stress was calculated by  
159 dividing the force by the initial cross-sectional area of the specimen. The sample thickness was  
160 measured in high-resolution mode of SEM with a resolution better than 10 nm. Videos with rate  
161 of 5 frames/sec were recorded and post-processed using home-made MATLAB scripts. The  
162 engineering strain was extracted by measuring the displacement directly in the gauge section of  
163 the specimen using digital image correlation (DIC). The effect of the electron beam on the  
164 mechanical response of the films was investigated by performing beam-off and beam-on PTP  
165 experiments with controlled electron doses at 200 kV and at 80 kV.

166

167 **3. Results**168 *a. PLD amorphous olivine characterization*

169 PLD  $\alpha$ -olivine films have already been the subject of chemical and microstructural  
170 characterizations [10, 16]. The selected area diffraction pattern (SAED) given in Fig. 2 shows the  
171 presence of two diffuse rings which confirms the amorphous structure. In this figure, a pair  
172 distribution function (PDF)  $G(r)$  calculated from the same SAED pattern shows two main peaks

173 located at 1.6 and 2 Å which corresponds to the Si-O and Mg-O medium range order (MRO),  
 174 respectively [19].

175

176 *b. in situ TEM nanomechanical testing*

177 Table 3 summarizes the characteristics of the PTP specimens used in the present work. It includes  
 178 the loading rate, the PTP stiffness, the specimen dimensions, the maximum engineering strain  
 179 and stress, the plastic strain at fracture, elastic modulus, the irradiation conditions (beam-on,  
 180 beam-off or alternating beam-on/beam-off) as well as the voltage and electron dose. The Poisson  
 181 ratio is equal to 0.5.

182 Fig. 3a presents in blue the variation of the engineering stress  $\sigma^{eng} = \frac{F}{A_0}$  ( $F$  is the applied force,  
 183  $A_0$  is the cross section area prior to deformation) as a function of the engineering strain  $\varepsilon^{eng} =$   
 184  $\frac{\Delta L}{L_0}$  ( $L_0$  being the gauge length of the dog bone specimen, see Fig. 3b) corresponding to OL-1  
 185 deformed at room temperature under load control mode (loading rate  $0.05 \mu\text{N}\cdot\text{s}^{-1}$ ) and beam-on  
 186 condition. At this stage, the only correction is related to the PTP stiffness. It is difficult to precisely  
 187 determine the yield point since the response bends progressively until a maximum engineering  
 188 stress of 1.69 GPa is reached at *ca.* 12.9 % engineering strain. This is followed by an apparent  
 189 softening regime which continues until rupture at 35.7 % engineering strain and 1.1 GPa  
 190 engineering stress. An apparent Young's modulus, named simply “elastic modulus”, was  
 191 determined, see Table 3, during loading using the slope from zero strain to the point at which a  
 192 deviation from the initial linear regime is detected. This gives a value of 69.2 GPa for the curve of  
 193 Fig. 3a. The maximum plastic strain, also reported in Table 3, is obtained by subtracting from the  
 194 total strain the elastic strain which is equal to the stress at fracture divided by the elastic modulus,  
 195 giving here 34 %. This very high ductility requires further stress and strain corrections to account  
 196 for dimensional variations of the specimen during deformation. As the deformation is followed *in*  
 197 *situ* in the microscope, the variation of the width can be measured during deformation, and, by  
 198 simply assuming that the deformation is isotropic in each transverse section, the following  
 199 correction is made (represented by the orange curve in Fig. 3a):

200 
$$\sigma^{true 2} = \frac{\sigma^{eng}}{(1+\varepsilon^T)^2} ; \varepsilon^{true 2} = \ln(1 + \varepsilon^{eng}) \quad \text{Eq. (1)}$$

201 where  $\varepsilon^T$  is the transverse strain. Fig. 3a indicates that the stress is affected by this correction  
202 leading to a higher value of the maximum stress (close to 2 GPa) while the true fracture strain is  
203 equal to 28.8 % which still demonstrates a high ductility when expressed with a logarithm norm.  
204 Figs. 3b, 3c and 3d show snapshots before deformation, just before and after fracture,  
205 respectively. Plasticity is very stable. Necking does not start after the maximum stress is reached.  
206 Also, there is no sign of catastrophic shear banding. Hence, the fracture strain is large. Only a very  
207 slight necking is observed just before fracture as can be seen in Fig. 3c (see Fig. S1 in the  
208 Supplementary Materials for more details on necking determination). Interestingly, the intensity  
209 profiles shown in Fig. 3e show that this late necking correlates with the formation of a nanovoid  
210 at the center of the gauge section indicating that the fracture is ultimately controlled by  
211 cavitation. This void can also be observed in the zoom of Fig. 3c. These observations raise the  
212 question of the origin of the apparent softening regime emerging from Fig. 3a (*i.e.* a decrease of  
213 the true stress value).

214 Figure 4a shows engineering stress-strain curves for OL-2 and OL-3 deformed without being  
215 exposed to the e-beam (beam-off) together with OL-1 with beam-on for comparison. All these  
216 experiments were performed under load-control mode with a loading rate of 0.05  $\mu\text{N/s}$ . In this  
217 figure, a clear increase of strength at the expense of ductility can be observed when the e-beam  
218 is switched off. Indeed, the maximum stress (resp. fracture strain) increases (resp. decreases)  
219 from 1.7 GPa (resp. 35.7 %) under beam-on to 2.4-2.6 GPa (resp. 28.9-17.3 %) under beam-off.  
220 The apparent modulus measured under beam-off was equal to 48.1 and 38.1 GPa for OL-2 and  
221 OL-3, respectively (69.2 GPa under beam-on). The corresponding plastic strains at fracture are  
222 given in Table 3. Figure 4b represents four deformation cycles imposed on OL-4 under load control  
223 mode with a loading rate of 0.1  $\mu\text{N/s}$  and under beam-off, in terms of engineering stress-strain  
224 response for each cycle. After each cycle, the experiment was stopped in order to set the  
225 parameters of the following cycle. The maximum load was increased after each cycle. An apparent  
226 Young's modulus of 40.1 GPa (Table 3) was extracted for the first cycle. No significant variation of  
227 the modulus between cycles was observed. Note that a significant forward creep contribution  
228 occurs upon unloading leading to a hysteresis in the response. This creep deformation is related  
229 to the viscoplastic behaviour of amorphous olivine, as further analyzed in the sequel. Fracture



230 occurred during the fourth cycle at an applied stress of 2.53 GPa and a total accumulated strain  
231 of 13.1 %. Figure 4b shows that plastic deformation accumulates during the cycles as evidenced  
232 by the deviation from the pure elastic regime detected at an applied stress of  $\sim 1.15$  GPa for cycle  
233 1, 2.07 GPa for cycles 2, 2.64 GPa for cycle 3, and 2.53 GPa for cycle 4. The fracture strain  
234 (expressed as total strain or plastic strain) varies from one specimen to another. This is not  
235 unexpected as the fracture strain heavily depends on the presence of defects.

236 Figures 5a and 5b show force-vs-time and displacement-vs-time curves from tensile  
237 experiment for OL-5 sample under alternating beam-on and beam-off conditions (every 5 min) at  
238 200 kV conducted in the load control mode. Figures 5c and 5d show data from a similar  
239 experiment performed at 80 kV on the OL-6 sample. The results show a clear decrease (resp.  
240 increase) of the force (resp. displacement) under beam-on (resp. beam-off) condition indicating  
241 the activation of viscoplasticity mechanisms under e-beam irradiation at 80 and 200 kV.

242

#### 243 *c. EELS measurements under e-beam irradiation*

244 An undeformed specimen of amorphous olivine was measured by EELS to probe the electron  
245 beam influence on its structure and properties (see Fig. 6 and Figs. S2, S3 and S4 in the  
246 Supplementary Materials). The study parameters are dose and voltage. EELS data acquired at 200  
247 keV are presented in Fig. 6 together with a comparison of the O K edge fine structure at 80, 200  
248 and 300 kV (Fig. 6e). Beam damage by electron beam can involve two mechanisms: (i) knock-on  
249 damage due to high-angle elastic electron-nucleus scattering which primarily concerns  
250 conductive materials and is all the more effective the higher the voltage; (ii) ionization damage  
251 called radiolysis due to low-angle inelastic electron-electron scattering which results in the  
252 breakup of covalent bonds, in the formation of electron-hole pairs in (semi)conductors or of  
253 radicals in organic materials and the creation of secondary electrons which may initiate further  
254 chemical reactions and further damage process. Radiolysis generally predominates at low  
255 acceleration voltage, when the incident beam energy is just above the ionization energy [20, 21].

256 At 80 kV, damage by radiolysis is the main mechanism as evidenced by the presence of a strong  
257 prepeak of the O K edge, at 530 eV, which corresponds to the immediate production and the  
258 liberation from the surface of molecular O<sub>2</sub> [22-25] (see Figs. S2a-b). This happens regardless of

259 the electron dose and ceases after some time of irradiation [23]. The Mg K edge was detected  
260 but disappears after less than a minute (see Fig. S3). This observation correlates with the  
261 disappearance during the first seconds of the measurement of a significant shoulder of the O K  
262 edge, which is attributed to the O-Mg bonds of forsterite character (fig 6e first panel). Another  
263 feature is the appearance of a shoulder at low energy (from 98 to 104 eV) on the Si L edge at high  
264 dose rate which might be a sign of some silicon with lower bonding covalency (Supplementary  
265 Fig. 2d). On the other hand, we can notice a progressive decrease of the Fe and the Si  
266 signals indicating a sputtering of heavy atomic species due to knock-on damage (see Fig. S2). In  
267 summary, in this compound, beam damage at 80 kV is mainly due to ionization, which  
268 predominantly affects Mg-O bonds and results in the departure of oxygen from the surface but  
269 not from the bulk. Some ablation of Mg from the bulk is also noted which must probably be  
270 attributed to knock-on. Ablation of Fe and Si by knock-on is also observed, but to a much lower  
271 extend.

272 At 300 kV, damage by knock-on is the dominant mechanism, as evidenced by the reduction of  
273 the signals of the different elements due to sputtering seen on Fig. S4. Mg is not detected so we  
274 suppose that it is the first element to be affected. No change of fine structure is observed, the  
275 order of ablation of the elements is as follows Mg>O>Fe>Si.

276 The least amount of damage is observed at 200 kV since the contribution of radiolysis reduces  
277 (see Fig. 6b). Indeed, we see no change of the fine structure of the O K edge throughout the  
278 measurement (left inset in Fig. 6b (I)). Departure of oxygen results predominantly from knock-on  
279 (Fig. 6e (II)). We can notice that beam showering (broad illumination of the specimen with an  
280 intense beam) at 80 kV removes the production of molecular oxygen (prepeak to the O K edge)  
281 but the fine structure of the O K edge is then similar to the spectrum at the end of the damage  
282 measurement (no more high energy shoulder). The Mg K edge could not be measured, but  
283 observation of the shoulder of the O K edge at low dose suggest ablation of Mg by knock-on. Si  
284 and Fe are ablated by knock-on, but much less than at 300 kV. The Si L edge does not seem to  
285 change throughout the measurement, (seen on Fig. 6c-d) showing that SiO<sub>4</sub> tetrahedra are little  
286 affected. In summary, at 200 kV, electron beam damage involves both mechanisms with a

287 stronger contribution of radiolysis at low dose and a stronger contribution of knock-on at high  
288 dose. In both cases, O and Mg are predominantly affected.

289

#### 290 **4. Discussion**

291 When the temperature is significantly lower than the glass transition temperature  $T_g$ , silicate  
292 glasses, like silica glass, are brittle solids. Only above  $T_g$  can they be shaped, as man has learned  
293 to do since the Bronze Age [26]. It is reasonable to assume that the same applies to a-olivine,  
294 although this glass is not available in bulk form. However, it has recently been shown on  
295 amorphous silica, whether on nanowires [27] or nanofibers [28], that significant ductility can be  
296 achieved at room temperature (i.e. far from  $T_g$ ) at small scales. This is not a unique property of  
297 silica, since amorphous alumina, for example, exhibits the same behavior [8]. We show here that  
298 the same is true for a-olivine, which can be strained up to almost 30 % at room temperature while  
299 its  $T_g$  is of the order of 1000 K [1, 29]. Plastic flow occurs at a stress of the order of 2.5 GPa. The  
300 cycles of the OL-4 experiment clearly show that the strain produced in the non-linear regime  
301 accumulates over the cycles and is indeed non-recoverable, plastic. These tests also show that  
302 creep deformation keeps accumulating during unloading, which will be discussed later. The  
303 observed apparent softening, is due to the response of the device (load controlled) to the  
304 evolution of the strain-rate (see Fig. S5 in the Supplementary Materials) and strongly depends on  
305 the strain-rate sensitivity of the specimen.

306 The mechanical properties of a-olivine have already been investigated at room temperature  
307 by using nanoindentation [30]. In this earlier work, the Young's modulus of a-olivine, was  
308 determined to be between 89 and 92 GPa. The values obtained under uniaxial tension with the  
309 PTP testing frame in the present work (see table 3) are lower than those obtained by  
310 nanoindentation [30]. Indeed, the elastic modulus extracted from the PTP experiments varies  
311 between 35 and 69 GPa. Aside from uncertainty on the exact thickness, the main source of error  
312 probably comes from sample misalignment. A small deviation from perfect alignment of the  
313 specimen axis with respect to the PTP pulling direction leads to significant impact on the apparent  
314 specimen stiffness. The fact that the length of the undeformed specimen is relatively short  
315 amplifies this effect. One must also add unperfect flatness of the specimen which contribute a lot

316 at small to moderate strain levels as the specimen gets progressively stretched. This why, again,  
317 other methods are more appropriate to get accurate Young's modulus, such as nanoindentation.  
318 The differences could also result from the activation of relaxation mechanisms at the very early  
319 stage of deformation in the PTP tensile experiments. Uncovering the origin of such behavior  
320 requires further investigations which go beyond the scope of the present study.

321 The striking feature of our experiments is the marked sensitivity of  $\alpha$ -olivine's mechanical  
322 properties to electron irradiation (Figs. 4 and 5). This phenomenon has already been revealed in  
323 amorphous silica, and has been the subject of several SEM and TEM studies [9, 31-33]. Under  
324 electron irradiation (at 200 kV), there is a significant drop (of around 0.7-1 GPa) in flow stress and  
325 a significant increase in ductility (Fig. 4). The latter can even reach spectacular levels when  
326 alternating beam on/beam off episodes are applied, as one test (at 80 kV) was conducted up to  
327 140 % elongation (without failure being reached). Figure 5 highlights the strain-rate dependent  
328 plastic flow of  $\alpha$ -olivine both under beam-off and beam-on conditions at both 80 and 200 kV with  
329 the same behavior being observed. Figures 5, b and d show that  $\alpha$ -olivine switches almost  
330 instantaneously (at the timescale of observation) between stiff and more ductile behavior, which  
331 is reflected in a change in slope of the displacement curve as a function of time. On the force vs.  
332 time curves (Figs. 5 a,c), this translates into a drop in stress as ductility increases. A similar  
333 enhancement of the viscoplastic flow activity due to the electron beam has been reported very  
334 recently on metal thin films using a specific MEMS device allowing for displacement-controlled  
335 experiment [34]. In this study, the stress relaxation occurring when the electron beam is turned  
336 on is consistent with a rate-controlling mechanism. It is more surprising here since the constant  
337 loading rate experiment should not induce stress relaxation but rather a larger creep  
338 contribution.

339 Such in-between stress relaxation and creep behavior is a direct consequence of the PTP setup.  
340 In order to interpret this phenomenon, and to extract the viscoplastic response of  $\alpha$ -olivine, we  
341 propose a simple 1D model aiming at simulating the mechanical response of olivine while taking  
342 into account the load transfer between the PTP and the sample. This model is described in the  
343 Supplementary Materials. The results are presented in Fig. 7 in terms of stress-strain curves and  
344 strain-time curves for experiments conducted at for 200 kV and 80 kV. The resulting rheological

345 parameters and PTP stiffness are summarized in Table 4. A fairly good agreement is found  
346 between the experimental data and the results of the 1D model. It confirms the hypothesis made  
347 for the mechanical behavior of  $\alpha$ -olivine, *i.e.* elastic-viscoplastic without any time-independent  
348 yield threshold. Both stress-relaxation and creep are very well reproduced. The peak stress is 50  
349 % higher in the case of the 200 kV acceleration voltage. On the contrary, strain rate and strain  
350 rate sensitivity are larger under 80 kV acceleration voltage. The strain rate sensitivity is equal to  
351 0.34 under irradiation at 200 kV, and equal to 0.55 under irradiation at 80 kV (Table 4). These very  
352 large values, typical of superplastic materials, can be compared with the strain-rate sensitivity  
353  $m = 0.05$  determined by nanoindentation [30] and from recent on-chip relaxation tests at very  
354 low strain rates down to  $10^{-12} \text{ s}^{-1}$  [16]. The strain-rate sensitivity is 6 to 10 times higher when  $\alpha$ -  
355 olivine is deformed under e-beam irradiation.

356 The mechanism by which electron irradiation promotes the ductility of  $\alpha$ -olivine may be open  
357 to question at 200 kV since our EELS measurements show that at this acceleration voltage two  
358 damage mechanisms, radiolysis and knock-on, operate. However, the fact that this effect is even  
359 more pronounced at 80 kV, where only radiolysis is active, leads us to conclude that the radiolysis  
360 mechanism is the cause of the enhanced ductility in  $\alpha$ -olivine. This process, which is specific to  
361 dielectrics, results from inelastic interaction between incoming electrons and atomic electrons.  
362 This induces local electron excitations or complete ionization which alters bonding between  
363 atoms, so that existing bonds could break leading to the formation of other bonds [35]. Radiolysis  
364 has mainly been studied in crystalline or amorphous silica where it leads to the formation of  
365 defects associated with broken bonds between silicon and oxygen atoms: silicon dangling bonds,  
366 oxygen deficiency centers, non-bridging oxygen hole centers [36, 37] and to the release of some  
367 oxygen molecules. This last defect is the one that gives the most discriminating signature in our  
368 EELS measurements (Fig. 6e). We find however that Si remains fourfold coordinated (Fig. 6c, d  
369 and Fig. S3c, d in the Supplementary Materials). On the other hand, it is mainly the Mg atoms  
370 (and therefore the Mg-O bonds) that are affected. To further investigate this point, we made a  
371 theoretical estimation of cross sections related to radiolytic processes. The radiolytic damage  
372 cross section, denoted by  $\sigma_r$ , can be expressed as  $\sigma_r = \zeta \sigma_e$ , as depicted in prior studies [35, 38-  
373 40]. Here,  $\zeta$  stands as the radiolytic efficiency factor, approximately equal to  $10^{-4}$  as reported in

374 literature [35], while  $\sigma_e$  encapsulates the cross section of a relativistic electron interacting with a  
 375 specimen electron:

$$376 \quad \sigma_e = \frac{8\pi a_0^2 R_\infty^2}{mc^2} \frac{Z}{T_{th}\beta^2}$$

377 In this expression,  $T_{th}$  denotes the dissociation energies ( $\sim 8.3$  eV for the Si-O bond,  $\sim 3.7$  eV for  
 378 the Mg-O bond [41]);  $Z$  represents the number of electrons surrounding the target;  $a_0$  symbolizes  
 379 the Bohr radius;  $mc^2$  signifies the rest mass of an electron; and  $R_\infty$  is the Rydberg constant.  
 380 Additionally,  $\beta$  is defined as:

$$381 \quad \beta = \sqrt{1 - \frac{1}{(U_b/mc^2 + 1)^2}}$$

382 with  $U_b$  being the incident beam energy.

383 Figure 8 shows that whatever the accelerating voltage, the radiolytic damage cross section is  
 384 larger for the Mg-O bonds. This demonstrates a larger sensitivity of those bonds to radiolytic  
 385 damage. Figure 8 shows also, as observed in our EELS measurements, a strongly increasing  
 386 efficiency of this damage mechanism as the acceleration voltage of electrons is reduced. We  
 387 therefore conclude that the electron beam assisted viscoplastic response of amorphous olivine is  
 388 mostly enhanced by the perturbation of the Mg-O bonds which facilitate the activation of plastic  
 389 events (in line with the shear transformation zones formalism, STZ, originally proposed by Argon  
 390 [42] and then named by Falk and Langer [43]). Because of the way viscoplasticity is promoted, the  
 391 role of electron irradiation can be compared with that of temperature. While these two  
 392 mechanisms may be equivalent in terms of behavior, they differ in their microscopic mechanisms.  
 393 Thermal activation provides the energy needed to overcome the barriers involved in plastic  
 394 events. Irradiation, on the other hand, lowers certain barriers through random inelastic  
 395 interactions. The activation of STZs leads to stress and strain redistribution which further assists  
 396 the thermal activation of new STZs [44]. As some simulations have shown, this coupling is likely  
 397 to induce organization leading to the formation of shear bands [45]. This coupling may play a  
 398 lesser role if the nucleation of plastic events is primarily determined by random interactions with  
 399 the electron beam leading to plastic delocalization. We can speculate that this is one possibility  
 400 to explain the very high stability of plastic deformation we observe up to very high strains. Further

401 advanced TEM are required to unravel possible links between these mechanisms and local  
402 fluctuation of the atomic density, the chemical composition or the local atomic order [46].

403

## 404 **5. Conclusion**

405 We show that a-olivine thin films exhibit a significant ductility at room temperature. Under tensile  
406 loading with the electron beam off, a maximum stress of about 2.5 GPa is attained and a strain of  
407 29 % can be reached. The stress-strain curve shows a stress maximum resulting from the response  
408 of the device to the increasing strain-rate with strain. The key finding of this study is the sensitivity  
409 of a-olivine to electron irradiation, which leads to a significant increase in ductility. An in-depth  
410 EELS study of the response of a-olivine under electron irradiation as a function of dose, but above  
411 all of acceleration voltage, led to the following conclusions. At low voltages (80 kV in our case),  
412 the predominant damage mechanism is radiolysis, clearly demonstrated by the release of  
413 molecular oxygen. At high voltages (300 kV), damage is mainly the result of knock-on that ablates  
414 the sample. The 200 kV voltage corresponds to the least damaging conditions for a-olivine since  
415 radiolysis is less than at 80 kV and knock-on is less than at 300 kV. The fact that irradiation  
416 enhanced ductility already observed at 200 kV is even more pronounced at 80 kV leads us to  
417 conclude that the mechanism responsible for this effect is radiolysis which promotes the breaking  
418 of Mg-O bonds.

419

## 420 **Data availability**

421 On reasonable request to the authors

422

## 423 **Declaration of Competing Interest**

424 The authors declare that they have no known competing financial interests or personal  
425 relationships that could have appeared to influence the work reported in this paper.

426

## 427 **Acknowledgements**

428 This project has received funding from the European Research Council (ERC) under the European  
429 Union's Horizon 2020 research and innovation programme under grant agreement No 787198 –  
430 TimeMan. H. Idrissi is mandated by the Belgian National Fund for Scientific Research (FSR- FNRS).  
431 This work was supported by the FNRS under Grant PDR –T011322F and the Programme 'Actions

432 de Recherche concertées (ARC) of the Fédération Wallonie-Bruxelles (re: project 'NanoGG' ref.  
433 nbr. 23/27-132).



434 **References**

- 435 [1] P. Richet, F. Leclerc, L. Benoist, L. Melting of forsterite and spinel, with implications for the  
436 glass transition of Mg<sub>2</sub>SiO<sub>4</sub> liquid. *J. Geophys. Res.* 20 (1993) 1675-1678.  
437 <https://doi.org/10.1029/93GL01836>
- 438 [2] R. Jeanloz, T.J. Ahrens, J.S. Lally, G.L. Nord, J.M. Christie, A.H. Heuer, Shock-Produced Olivine  
439 Glass: First Observation. *Science*, 197 (1977) 457-459.  
440 <https://doi.org/10.1126/science.197.4302.457>
- 441 [3] A. Lacam, M. Madon, J.P. Poirier, Olivine glass and spinet formed in a laser heated, diamond-  
442 anvil high pressure cell. *Nature* 288 (1977) 155-157. <https://doi.org/10.1038/288155a0>
- 443 [4] J. Gasc, S. Demouchy, F. Barou, S. Koizumi, P. Cordier. Creep mechanisms in the lithospheric  
444 mantle Inferred from deformation of iron-free forsterite aggregates at 900-1200 °C.  
445 *Tectonophysics*, 761 (2019) 16-30. <https://doi.org/10.1016/j.tecto.2019.04.009>
- 446 [5] H. Idrissi, P. Carrez, P. Cordier, On amorphization as a deformation mechanism under high  
447 stresses. *Curr. Opin. Solid State. Mater. Sci.* 26(1) (2022) 100976.  
448 <https://doi.org/10.1016/j.cossms.2021.100976>
- 449 [6] V. Samae, P. Cordier, S. Demouchy, C. Bollinger, J. Gasc, S. Koizumi, A. Mussi, D. Schryvers, H.  
450 Idrissi, Stress-induced amorphization triggers deformation in the lithospheric mantle. *Nature* 591  
451 (2021) 82–86. <https://doi.org/10.1038/s41586-021-03238-3>
- 452 [7] G. Kermouche, G. Guillonueau, J. Michler, J. Teisseire, E. Barthel, Perfectly plastic flow in silica  
453 glass, *Acta Mat.* 114 (2016) 146-153. <http://dx.doi.org/10.1016/j.actamat.2016.05.027>
- 454 [8] E. J. Frankberg, J. Kalikka, F.G. Ferré, L. Joly-Pottuz, T. Salminen, J. Hintikka, M. Hokka, S. Koneti,  
455 T. Douillard, B. Le Saint, P. Kreiml, M.J. Cordill, T. Epicier, D. Stauffer, M. Vanazzi, L. Roiban, J.  
456 Akola, F. Di Fonzo, E. Levänen, K. Masenelli-Varlot, Highly ductile amorphous oxide at room  
457 temperature and high strain rate. *Science* 366 (2019) 864–869.  
458 <https://doi.org/10.1126/science.aav1254>
- 459 [9] K. Zheng, C. Wang, Y.Q. Cheng, Y. Yue, X. Han, Z. Zhang, Z. Shan, S.X. Mao, M. Ye, Y. Yin, E. Ma,  
460 Electron-beam-assisted superplastic shaping of nanoscale amorphous silica. *Nature Comm.* 1  
461 (2010) 24. <https://doi.org/10.1038/ncomms1021>

- 462 [10] R. Dohmen, H.-W. Becker, E. Meißner, T. Etzel, S. Chakraborty, Production of silicate thin  
463 films using pulsed laser deposition (PLD) and applications to studies in mineral kinetics, Eur. J.  
464 Mineral. 14 (2002) 1155–1168. <https://doi.org/10.1127/0935-1221/2002/0014-1155>.
- 465 [11] T. Egami, S.J.L. Billinge, Underneath the Bragg Peaks: Structural Analysis of Complex  
466 Materials; Pergamon Press: Oxford, UK; Elsevier: Amsterdam, The Netherlands (2003).
- 467 [12] P. Juhas, T. Davis, C. L. Farrow, S.J.L. Billinge, *PDFgetX3*: a rapid and highly automatable  
468 program for processing powder diffraction data into total scattering pair distribution functions. J.  
469 Appl. Cryst., 46 (2013) 560-566. <https://doi.org/10.1107/S0021889813005190>
- 470 [13] e-PDFSuite–Software for Analysis of Amorphous and Nano Crystalline Materials.  
471 NanoMEGAS SPRL: Belgium, 2009.
- 472 [14] M. Abeykoon, C.D. Malliakas, P. Juhás, E.S. Božin, M.G. Kanatzidis, S.J.L. Billinge, Quantitative  
473 nanostructure characterization using atomic pair distribution functions obtained from laboratory  
474 electron microscopes. Z. für Krist. 227 (2012) 248–256. <https://doi.org/10.1524/zkri.2012.1510>
- 475 [15] Y. Rakita, J.M. Hart, P.P. Das, S. Shahrezaei, D.L. Foley, S.N. Mathaudhu, S. Nicolopoulos, M.L.  
476 Taheri, S.J.L. Billinge, Mapping structural heterogeneity at the nanoscale with scanning nano-  
477 structure electron microscopy (SNEM), Acta Mat., 242 (2023) 118426.  
478 <https://doi.org/10.1016/j.actamat.2022.118426>
- 479 [16] M. Coulombier, P. Baral, A. Orekhov, R. Dohmen, J-P. Raskin, T. Pardoën, P. Cordier, H. Idrissi,  
480 On-chip very low strain rate rheology of amorphous olivine films, Acta Mat. 266 (2024), 119693,  
481 <https://doi.org/10.1016/j.actamat.2024.119693>
- 482 [17] M. Ghidelli, A. Orekhov, A. Li Bassi, G. Terraneo, P. Djemia, G. Abadias, M. Nord, A. Béché, N.  
483 Gauquelin, J. Verbeeck, J.P. Raskin, D. Schryvers, T. Pardoën, H. Idrissi, Novel class of  
484 nanostructured metallic glass films with superior and tunable mechanical properties, Acta Mat.  
485 213 (2021) 116955, <https://doi.org/10.1016/j.actamat.2021.116955>.
- 486 [18] V. Samae, R. Gatti, B. Devincere, T. Pardoën, D. Schryvers, H. Idrissi, Dislocation driven  
487 nanosample plasticity new insights from quantitative *in situ* TEM tensile testing, Sci. Rep. 8 (2018)  
488 12012, <https://doi.org/10.1038/s41598-018-30639-8>.

- 489 [19] B. Mantsi, N. Sator, B. Sator, Structure and transport at grain boundaries in polycrystalline  
490 olivine: An atomic-scale perspective. *Geochim. Cosmochim. Acta* 219 (2017) 160–176.  
491 <https://doi.org/10.1016/j.gca.2017.09.026>
- 492 [20] N. Jiang, Electron beam damage in oxides: a review, *Rep. Prog. Phys.* 79, 2016, 016501.  
493 <https://doi.org/10.1088/0034-4885/79/1/016501>
- 494 [21] R.F. Egerton, Radiation damage to organic and inorganic specimens in the TEM, *Micron* 119  
495 (2019) 72-87. <https://doi.org/10.1016/j.micron.2019.01.005>
- 496 [22] S.K. Lee, J.F. Stebbins, The degree of aluminum avoidance in aluminosilicate glasses, *Am. Min.*  
497 84 (1999) 937-945. <https://doi.org/10.2138/am-1999-5-631>
- 498 [23] L.A.J. Garvie, Can electron energy-loss spectroscopy (EELS) be used to quantify hydrogen in  
499 minerals from the O K edge?, *Am. Min.* 95 (2010) 92-97. <https://doi.org/10.2138/am.2010.3290>
- 500 [24] B. Winkler M Avalos-Borja, V Milman, A Perlov, C J Pickard, J R Yates, Oxygen K-edge electron  
501 energy loss spectra of hydrous and anhydrous compounds, *J. Phys.: Condens. Matter* 25 (2013)  
502 485401. <https://doi.org/10.1088/0953-8984/25/48/485401>
- 503 [25] H. O. Ayoola, C-H Li, S. D. House, C.S. Bonifacio, K. Kisslinger, J. Jinschek, W.A. Saidi, J. C. Yang,  
504 Origin and Suppression of Beam Damage-Induced Oxygen-K Edge Artifact from  $\gamma$ -Al<sub>2</sub>O<sub>3</sub> using Cryo-  
505 EELS, *Ultramicroscopy* (2020) 113127. <https://doi.org/10.1016/j.ultramic.2020.113127>
- 506 [26] H. Tait, Five thousand years of glass, British Museum press, London, 1991
- 507 [27] Y. Yue, K. Zheng, Strong strain rate effect on the plasticity of amorphous silica nanowires.  
508 *Appl. Phys. Lett.* 104 (2014) 231906. <https://doi.org/10.1063/1.4882420>
- 509 [28] J. Luo, J. Wang, E. Bitzek, J.Y. Huang, H. Zheng, L. Tong, Q. Yang, J. Li, S.X. Mao, Size-Dependent  
510 Brittle-to-Ductile Transition in Silica Glass Nanofibers. *NanoLetters* 16 (2016) 105-113.  
511 <http://dx.doi.org/10.1021/acs.nanolett.5b03070>
- 512 [29] J.A. Tangeman, B.L. Phillips, A. Navrotsky, J.K.R. Weber, A.D. Wilson, T.S. Key, Vitreous  
513 forsterite (Mg<sub>2</sub>SiO<sub>4</sub>): synthesis, structure and thermochemistry. *Geophys. Res. Lett.* 28 (2001)  
514 2517-2520. <https://doi.org/10.1029/2000GL012222>
- 515 [30] P. Baral, A. Orekhov, R. Dohmen, M. Coulombier, J.-P. Raskin, P. Cordier, H. Idrissi, T. Pardoën,  
516 Rheology of amorphous olivine thin films characterized by nanoindentation, *Acta Mat.* 219 (2021)  
517 117257, <https://doi.org/10.1016/j.actamat.2021.117257>

- 518 [31] A.J. Storm, J.H. Stern, X.S. Ling, H.W. Zandbergen, C. Dekker, Electron-beam induced  
519 deformations of SiO<sub>2</sub> nanostructures. J. Appl. Phys. 98 (2005) 014307.  
520 <https://doi.org/10.1063/1.1947391>
- 521 [32] M. Mačković, F. Niekiel, L. Wondraczek, E. Spiecker, Direct observation of electron-beam-  
522 induced densification and hardening of silica nanoballs by *in situ* transmission electron  
523 microscopy and finite element method simulations. Acta Mat. 79 (2014) 363-373.  
524 <https://doi.org/10.1016/j.actamat.2014.05.046>
- 525 [33] S.G. Kang, K. Jeong, J. Paeng, W. Jeong, S. Han, J.P. Ahn, S. Boles, H.N. Han, I.S. Choi. Athermal  
526 glass work at the nanoscale: Engineered electron-beam-induced viscoplasticity for mechanical  
527 shaping of brittle amorphous silica. Acta Mat. 238 (2022) 118203.  
528 <https://doi.org/10.1016/j.actamat.2022.118203>
- 529 [34] S. Stangebye, Y. Zhang, S. Gupta, T. Zhu, O. Pierron, J. Kacher, Understanding and quantifying  
530 electron beam effects during *in situ* TEM nanomechanical tensile testing on metal thin films. Acta  
531 Mat. 222 (2022) 117441. <https://doi.org/10.1016/j.actamat.2021.117441>
- 532 [35] L.W. Hobbs, Electron-beam sensitivity in inorganic specimens. Ultramicroscopy, 23 (1987)  
533 339-344. [https://doi.org/10.1016/0304-3991\(87\)90244-0](https://doi.org/10.1016/0304-3991(87)90244-0)
- 534 [36] D.L. Griscom, Nature of defects and defect generation in optical glasses. Proc. Soc. Photo-  
535 Opt. Instrum. Eng. 541 (1985) 38–59. <https://doi.org/10.1117/12.975358>
- 536 [37] K. Kajihara, M. Hirano, L. Skuja, H. Hosono, Intrinsic defect formation in amorphous SiO<sub>2</sub> by  
537 electronic excitation: Bond dissociation versus Frenkel mechanisms. Phys. Rev. B 78 (2008)  
538 094201. <https://doi.org/10.1103/PhysRevB.78.094201>
- 539 [38] L.W. Hobbs, Radiation Effects in Analysis of Inorganic Specimens by TEM, in: J.J. Hren, J.I.  
540 Goldstein, D.C. Joy (Eds.), Introduction to Analytical Electron Microscopy, Springer US, Boston,  
541 MA, 1979, pp. 437-480.
- 542 [39] C.F. Blanford, C.B. Carter, Electron radiation damage of MCM-41 and related materials,  
543 Microsc. Microanal. 9(3) (2003) 245-63. <https://doi.org/10.1017/S1431927603030447>
- 544 [40] J. Lin, C. Grygiel, A. Alessi, S. Dourdain, J. Causse, N. Ollier, O. Cavani, C. Rey, G. Toquer, X.  
545 Deschanel, A multiparametric study on the behavior of mesoporous silica under electron  
546 irradiation, Materialia 32 (2023) 101903. <https://doi.org/10.1016/j.mtla.2023.101903>

- 547 [41] J. B. Pedley, E. M. Marshall, Thermochemical Data for Gaseous Monoxides; J. Phys. Chem.  
548 Ref. Data 12 (1983) 967–1031. <https://doi.org/10.1063/1.555698>
- 549 [42] A.S. Argon, Plastic deformation in metallic glasses, Acta Metall. 27 (1979) 47.  
550 [https://doi.org/10.1016/0001-6160\(79\)90055-5](https://doi.org/10.1016/0001-6160(79)90055-5)
- 551 [43] M.L. Falk & J.S. Langer, Dynamics of viscoplastic deformation in amorphous solids, Phys. Rev.  
552 E 57 (1998) 7192. <https://doi.org/10.1103/PhysRevE.57.7192>
- 553 [44] T. Albaret, A. Tanguy, F. Boioli, D. Rodney, Mapping between atomistic simulations and  
554 Eshelby inclusions in the shear deformation of an amorphous silicon model. Phys. Rev. E 93 (2016)  
555 053002. <http://dx.doi.org/10.1103/PhysRevE.93.053002>
- 556 [45] E.R. Homer, Examining the initial stages of shear localization in amorphous metals. Acta Mat.  
557 63 (2014) 44–53. <http://dx.doi.org/10.1016/j.actamat.2013.09.050>
- 558 [46] H. Idrissi, M. Ghidelli, A. Béché, S. Turner, S. Gravier, J.J. Blandain, J.P. Raskin, D. Schryvers,  
559 T. Pardoen, Atomic-scale viscoplasticity mechanisms revealed in high ductility metallic glass films,  
560 Sci. Rep. 9 (2019) 13426, <https://doi.org/10.1038/s41598-019-49910-7>
- 561

562 **Tables**

563

564

565

566

Voltage	SS14		SS17	
	Probe diameter (Å)	Beam current (pA)	Probe diameter (Å)	Beam current (pA)
80 kV	8	260	2.8	40
200 kV	6.5	360	2	50
300 kV	4	440	1.5	80

567

568 **Table 1.** Maximum probe diameters (in Angstroms) corresponding to EELS measurements. SS14

569 corresponds to spot size 14, SS17 corresponds to spot size 17.

570

571

572

573

Voltage	SS14	SS17
	Electron dose rate (e <sup>-</sup> /nm <sup>2</sup> /s)	Electron dose rate (e <sup>-</sup> /nm <sup>2</sup> /s)
80 kV	8.16 10 <sup>8</sup>	1.54 10 <sup>7</sup>
200 kV	7.46 10 <sup>8</sup>	9.80 10 <sup>6</sup>
300 kV	3.45 10 <sup>8</sup>	8.82 10 <sup>6</sup>

574

575 **Table 2.** Electron dose corresponding to the EELS measurements. SS14 corresponds to spot size

576 14, SS17 corresponds to spot size 17.

577

578

579

Label	Beam Mode	Load rate ( $\mu\text{N/s}$ )	PTP stiffness (N/m)	Sample dimensions (nm) Length / width / thickness	Max eng strain (%)	Max plastic strain (%)	Max eng stress (GPa)	Elastic modulus (GPa)	HT (kV)	Beam current (nA)	Electron dose rate ( $\text{e} \text{ \AA}^{-2}\text{s}^{-1}$ )
OL-1	On	0.05	269	2156 / 408 / 260	35.7	34	1.69	69.2	200	0.173	0.01
OL-2	Off	0.05	261	2094 / 395 / 260	28.9	24	2.39	48.1	200	-	-
OL-3	Off	0.05	286	1700 / 456 / 260	17.3	11	2.59	38.1	200	-	-
OL-4	Off, Cycles	0.1	469	1470 / 405 / 260	13.1	6.8	2.65	40.1 C1 41.9 C2 41.2 C3 40.3 C4	200	-	-
OL-5	On / Off	0.1	449	1500 / 460 / 270	68.1	64.4	1.51	37.8	200	2.47	0.11
OL-6	On / Off	0.05	204	1170 / 415 / 270	139	137.6	0.83	33.8	80	2.26	0.38

580

581 **Table 3.** Summarized technical data for all the PTP tensile experiments described in this study.

582

583

584

585

Acceleration voltage U	PTP stiffness (fitted) (N/m)	Consistency K ( $\text{GPa}\cdot\text{s}^{-\text{m}}$ )	Strain rate sensitivity $m$
80 kV (OI-6)	235	71	0.55
200 kV (OI-5)	500	26	0.34

586

587 **Table 4.** PTP stiffness, Consistency parameter K and strain rate sensitivity  $m$  for alternating beam-off/beam-on for acceleration voltage 80 kV and 200 kV.

588

589

590

591 **Figures**

592

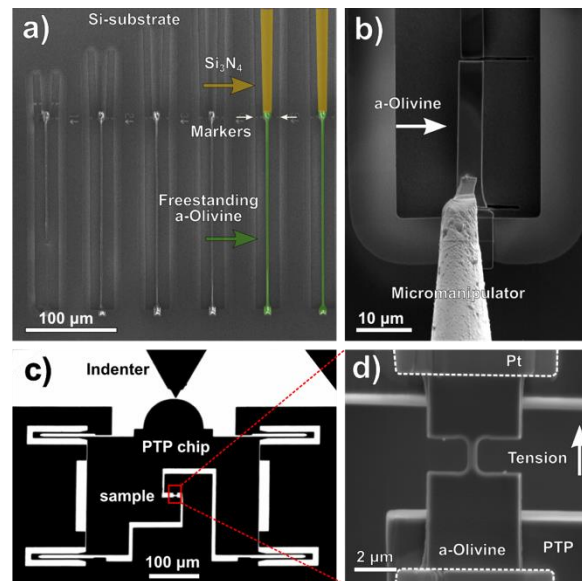
593

594

595

596

597



598

599 **Fig. 1.** a) SEM image of a freestanding amorphous olivine film (highlighted with green) and Si<sub>3</sub>N<sub>4</sub>  
 600 actuator (highlighted with yellow) on a lab-on-chip system before release (i.e. tensile  
 601 deformation); see the cursors indicated by the white markers in (a); Coulombier *et al.* (2024) b)  
 602 Magnified SEM image showing the transfer of a-olivine freestanding film on a PTP chip by a  
 603 micromanipulator. c) TEM overview image of PTP chip with a-olivine sample located in center as  
 604 shown in the magnified SEM image in (d).

605

606

607

608

609

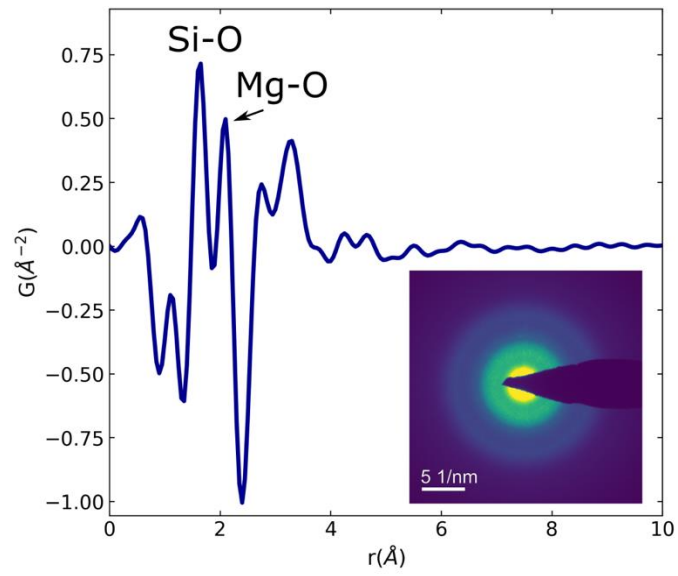
610

611

612



613



614

615 **Fig. 2.** Structure of the amorphous olivine film deposited by pulsed laser deposition (PLD). Pair  
616 distribution function (PDF),  $G(r)$ , calculated from the selected area electron diffraction (SAED)  
617 pattern in insert.

618

619

620

621

622

623

624

625

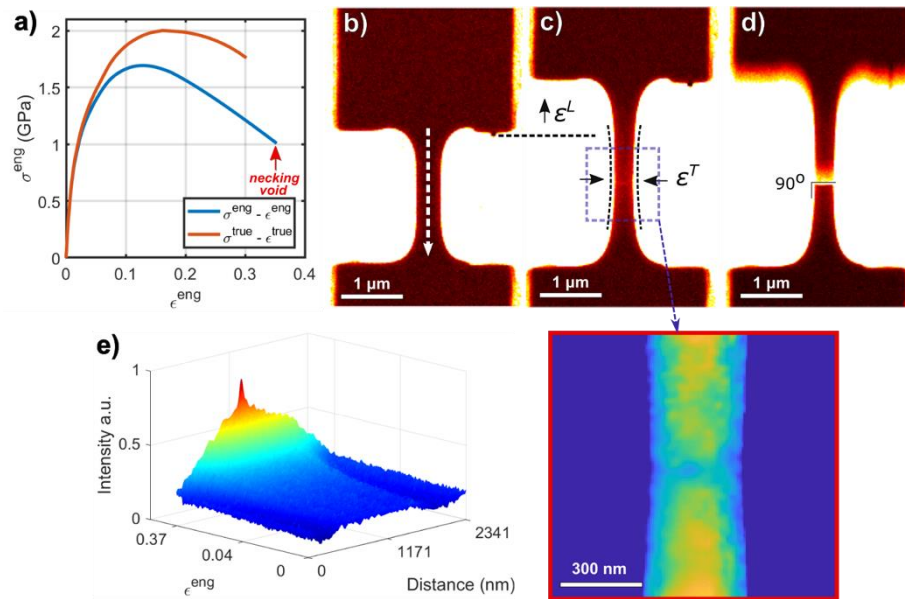
626

627

628

629

630



631  
 632  
 633 **Fig. 3.** a) Stress-strain curves (OL-1) calculated for engineering strain measurements (blue curve)  
 634 and true stress-strain curve calculated when transverse strain is measured (orange curve). The  
 635 red arrow indicates the simultaneous occurrence of necking and cavitation. b-d) Video snapshots  
 636 before deformation, just before and after fracture. e) Intensity profile measured along dashed  
 637 line in (b) shows the formation of a nanovoid at the center of the gage as function of the  
 638 engineering strain.

639

640

641

642

643

644

645

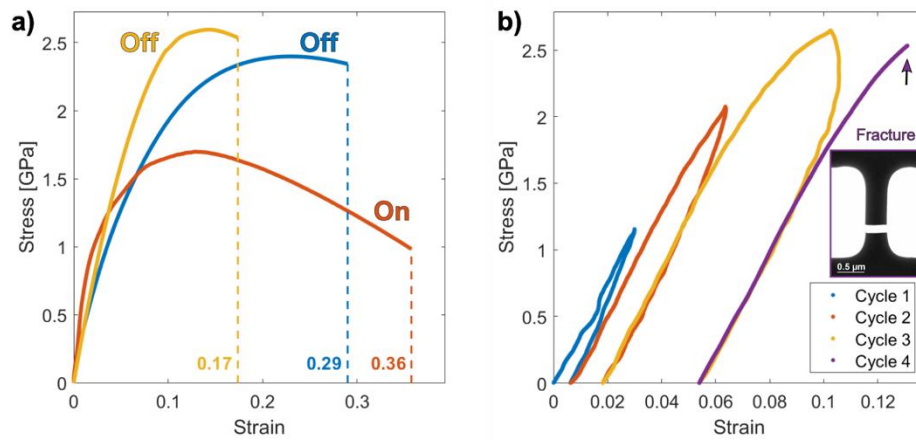
646

647

648

649

650



651

652 **Fig. 4.** a) Engineering stress-strain curves of 'beam on' (OL-1 orange) and 'beam off' (OL-2 blue  
653 and OL-3 yellow) experiments. b) Engineering stress-strain cycles of the 'beam off' (OL-4) sample.

654

655

656

657

658

659

660

661

662

663

664

665

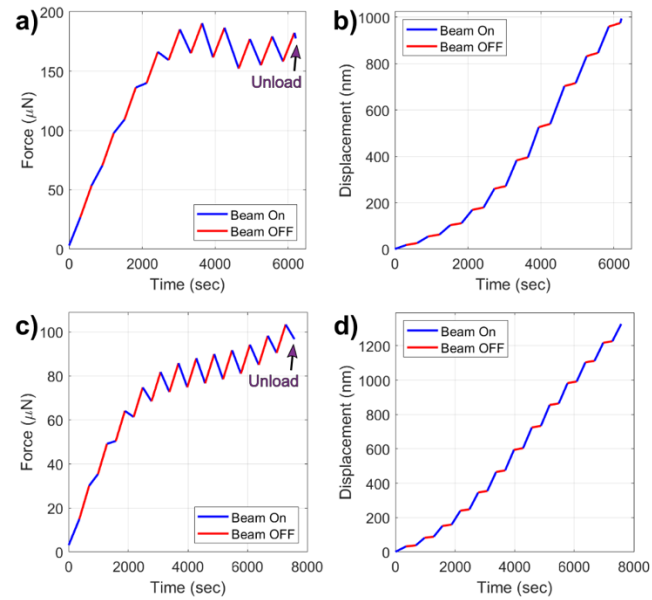
666

667

668

669

670



671

672 **Fig. 5.** PTP experiments performed at 200 kV and 80 kV with alternating beam On/Off every 5  
673 min. (a,b) Dependence of the force and displacement applied on the sample as a function of time  
674 at 200 kV (sample OL-5). (c,d) Dependence of the force and displacement applied on the sample  
675 as a function of time at 80 kV (sample OL-6).

676

677

678

679

680

681

682

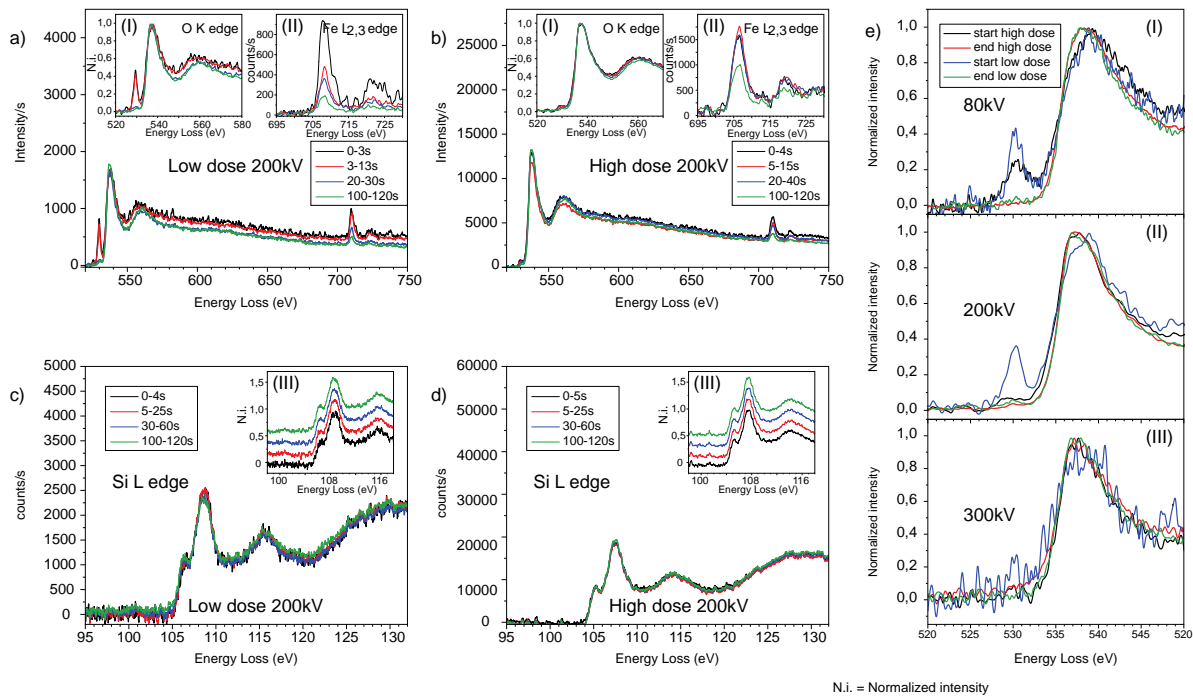
683

684

685

686

687



688

689 **Fig. 6.** a-b) EELS spectra recorded at low dose (SS17) and high dose (SS14) respectively at 200kV  
 690 acceleration voltage. In each panel, the main graph represents the O K edge together with the Fe  
 691 L edge in intensity per second, for 4 different periods during the measurement. The left inset (I)  
 692 represents the O K edge fine structure evolution (the intensity has been normalized for easier  
 693 comparison). The second inset (II) represents the Fe L edge in counts/second to identify the  
 694 depletion in Fe. c-d) Silicon L edge EELS spectra recorded at low dose (SS17) and high dose (SS14)  
 695 respectively. In each panel, the main graph represents the Si L edge in intensity per second, for 4  
 696 different periods during the measurement. The inset (III) represents the Si L edge fine structure  
 697 evolution (the intensity has been normalized for easier comparison). e) Direct comparison of the  
 698 O K edge ELNES recorded at low dose and high dose at the 3 different acceleration voltages (80,  
 699 200 and 300 kV from top to bottom) on amorphous olivine. For each experiment, a spectrum  
 700 taken at the start of the experiment and at the end of the experiment were extracted.

701

702

703

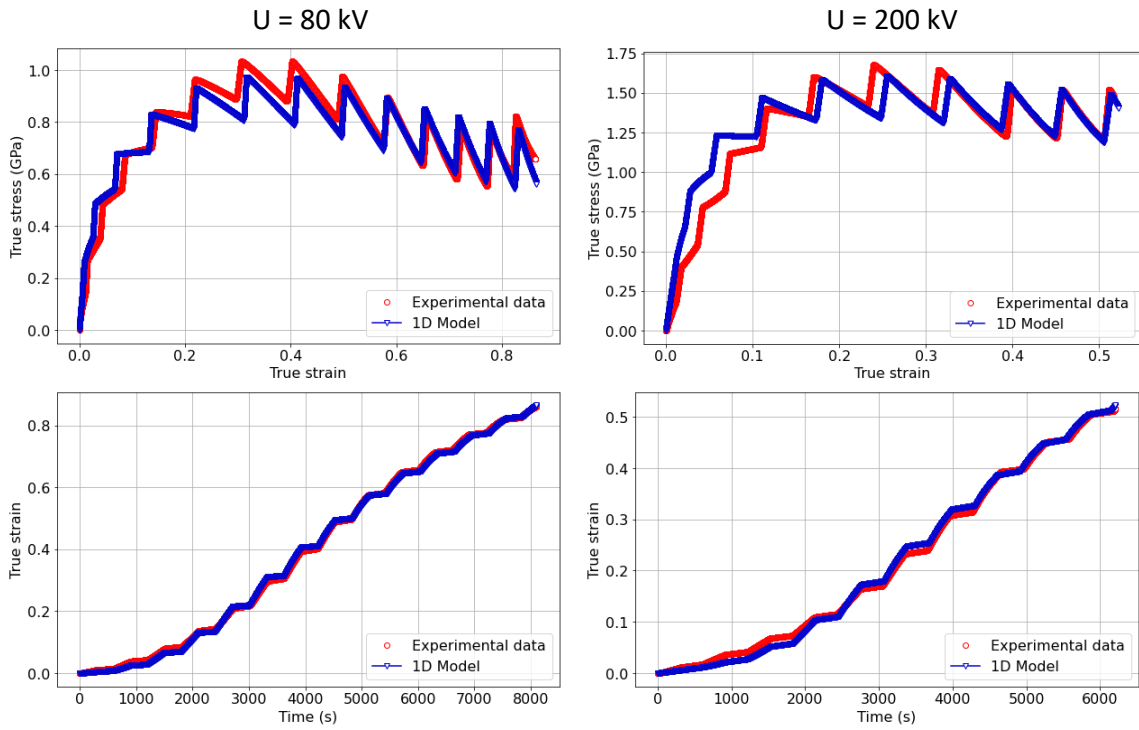
704

705

706

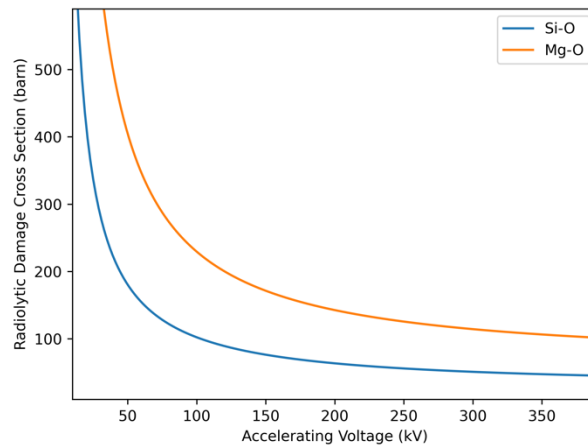
707

708



709  
 710 **Fig. 7.** comparison of experimental and numerical results of alternating beam-off/beam-on.  
 711 Acceleration voltage (left: 80 kV (OI-6) and right: 200 kV (OI-5)).  
 712

713  
 714  
 715



716  
 717 **Fig. 8.** Radiolytic cross section for Mg-O and Si-O bonds versus the kinetic energy of electrons.  
 718